

Research



Cite this article: Krsmanovic M, Ghosh R, Dickerson AK. 2023 Fur flutter in fluid flow fends off foulers. *J. R. Soc. Interface* **20**: 20230485.
<https://doi.org/10.1098/rsif.2023.0485>

Received: 18 August 2023

Accepted: 13 November 2023

Subject Category:

Life Sciences—Physics interface

Subject Areas:

biomechanics

Keywords:

animal hair, anti-fouling, filament topography, flow-induced vibrations, inorganic suspension

Author for correspondence:

Andrew K. Dickerson

e-mail: ad@utk.edu

Fur flutter in fluid flow fends off foulers

Milos Krsmanovic¹, Ranajay Ghosh¹ and Andrew K. Dickerson²

¹Department of Mechanical and Aerospace Engineering, University of Central Florida, Orlando, FL, USA

²Department of Mechanical, Aerospace, and Biomedical Engineering, University of Tennessee, Knoxville, TN, USA

MK, 0000-0003-1346-3672; AKD, 0000-0003-1220-1048

The fouling of submerged surfaces detrimentally alters stratum properties. Inorganic and organic foulers alike attach to and accumulate on surfaces when the complex interaction between numerous variables governing attachment and colonization is favourable. Unlike naturally evolved solutions, industrial methods of repellence carry adverse environmental impacts. Mammal fur demonstrates high resistance to fouling; however, our understanding of the intricacies of such performance remains limited. Here, we show that the passive trait of fur to dynamically respond to an external flow field dramatically improves its anti-fouling performance over that of fibres rigidly fixed at both ends. We have previously discovered a statistically significant correlation between a group of flow- and stratum-related properties, and the quantified anti-fouling performance of immobile filaments. In this work, we improve the correlation by considering an additional physical factor, the ability of hair to flex. Our work establishes a parametric framework for the design of passive anti-fouling filamentous structures and invites other disciplines to contribute to the investigation of the anti-fouling prowess of mammalian interfaces.

1. Introduction

Submerged surfaces are exposed to microorganisms, organic and inorganic matter which is apt to attach, accumulate and colonize [1–3]. The stratum transformations caused by contaminant attachment are typically detrimental, and in applications such as food and pharmaceuticals, often degrade the surrounding liquid media [4,5]. The attachment process, known as fouling, can be as simple as the sedimentation of particles suspended in the liquid [6], or as complex as the envelopment of microbes in an extracellular polymeric substance (EPS), as is the case with biofouling [7]. Generally, fouling is a complicated process, influenced by more than two dozen physico-chemical, mechanical, biological and other factors [8].

Industrial methods of fouler removal are numerous; however, they often employ harmful chemicals [9,10], consume energy [11–13] and/or materials [4,14,15]. In comparison, naturally evolved anti-fouling is typically passive [16,17] and, thus, advantageous in terms of ecological impacts and may provide anti-fouling strategies not currently employed. Submerged surfaces are particularly susceptible to organic and inorganic colonization, as liquid facilitates the transport of foulers and nutrients [18,19]. Certain animal and plant species evolved characteristics such as surface micro-patterns that increase the adhesion barrier for attachment. Classical patterning strategies include shark skin, which creates a unique boundary layer structure, and superhydrophobic lotus leaves [17,20,21]. There exists, however, an example of outstanding fouler repulsion still largely unexplored: mammalian fur. Apart from scarce evidence to the contrary [22], animal fur is widely observed to remain clean after being routinely submerged or wetted, an observation made across a wide array of species, climates and morphologies. Still, the physical underpinnings of fur anti-fouling performance remain obfuscated. Anti-fouling performance is affected by characteristics across multiple scales, from host dynamics and behaviour at the metre scale, to substrate dynamics at the millimetre scale and down to micrometre-scale surface texture [23]. The scales across which anti-fouling must be considered are illustrated in figure 1.

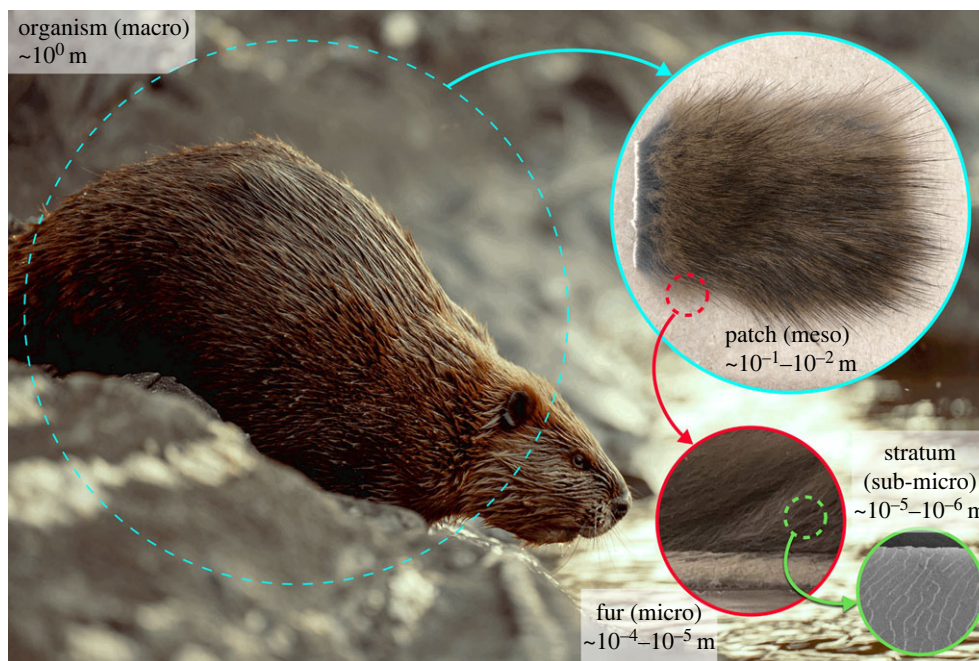


Figure 1. Mammal furs, such as that of American beaver (*Castor canadensis*), resist fouling by passive, multi-scale mechanisms ranging from the host scale to surface microscale. Photo by Tim Umphreys [24].

In previous work [25], we investigated the fur anti-fouling behaviour of six mammal species representing both semi-aquatic and terrestrial mammal orders, and two artificial fibres comparable in diameter to hair. All test fibres were fixed at both ends and exposed to cross-flow rich with TiO_2 particles for 24 h. We measured the accumulation of TiO_2 after exposure and found the amount of fouling does not correspond to any single system variable. Instead, a dimensionless group comprising physico-mechanical factors related to flow and filament surface properties is needed to predict fouling intensity. We considered fibre curvature $1/R$ (mm^{-1}), time of sample exposure to the fouler stream t (s), the concentration of particles in the liquid media c (l^{-1}), bulk velocity upstream of the fibre U (m s^{-1}), dynamic viscosity of the liquid μ (Pa s), liquid density ρ (kg m^{-3}), fibre circularity \emptyset (—), non-dimensional surface features factor ϵ (—) and surface shear stress τ_w (Pa). We considered the ratio of the stream inertial and viscous forces, the Reynolds number, as $\text{Re}_R = \rho U R / \mu$ (—). Using non-dimensional parametrization we establish statistically significant correlations for the surface normalized fouling intensity number N_P^* (mm^{-2}), the number of particles captured per square millimetre

$$N_P^* \left(\frac{1}{R} \right)^{-2} = f \left[\frac{1}{\text{Re}_R}, U \left(\frac{1}{R} \right) t, \frac{c}{\left(\frac{1}{R} \right)^3}, \emptyset, \epsilon, \frac{\tau_w}{\rho U^2} \right] \quad (1.1)$$

and

$$\underbrace{N_P^* \left(\frac{1}{R} \right)^{-2}}_{\Gamma} \sim \underbrace{\text{Re}_R \left(\frac{1}{R} \right)^{-2} \emptyset \epsilon \left(\frac{\tau_w}{\rho U} \right) t c}_{\Pi_T}, \quad (1.2)$$

such that

$$\Gamma \sim \Pi_T. \quad (1.3)$$

Correlations for furs submerged in flowing (figure 2a) and near-quiescent (figure 2b) liquids showed a demarcation between different fibre groups. Terrestrial mammal furs generally fouled more in our fouler stream than did semi-aquatic fur fibres, a difference more pronounced in quiescent liquid, a relation which cannot be established when correlating N_P^* with any other known parameter in isolation. Instead, the fouling process is driven by a number of factors in concert and whose influences may be more or less dominant in different flow or particle regimes. The correlation provided by (1.3) is statistically significant when applied to experiments performed with fibres fixed at both ends. In this current study, we perform similar experiments but push our experimental system closer to natural behaviour by fixing fibres only at one end, thereby permitting the flowing liquid to induce motion, or flutter, as it might in the natural system. Our motive is to continue to unravel the mechanisms by which furs passively resist fouling by nature of their morphology, dynamics and collective behaviour. We present our experimental methods in §2. We present fouling results and make comparisons with previous results in §3. Therein we also present modelling considerations for slender fibres permitted to deform in a flow field. We conclude our work in §4.

2. Materials and experimental methods

The materials and experimental methods in this study closely follow those described in our previous work, Krsmanovic *et al.* [25]. Here, we present the principal characteristics, and detail only the significant differences between the preceding and current works. We test three fibre types: American beaver (*Castor canadensis*), coyote (*Canis latrans*) and polypropylene (PP), representing three principal groups: semi-aquatic mammal fibres, terrestrial mammal fibres and artificial fibres, respectively. As noted in §1, these fibres have been selected to represent diverse origins and topographical characteristics, and in the case of animal fur, natural habitats and body sizes. We demonstrate that certain fibre materials and mounting configurations exhibit significantly

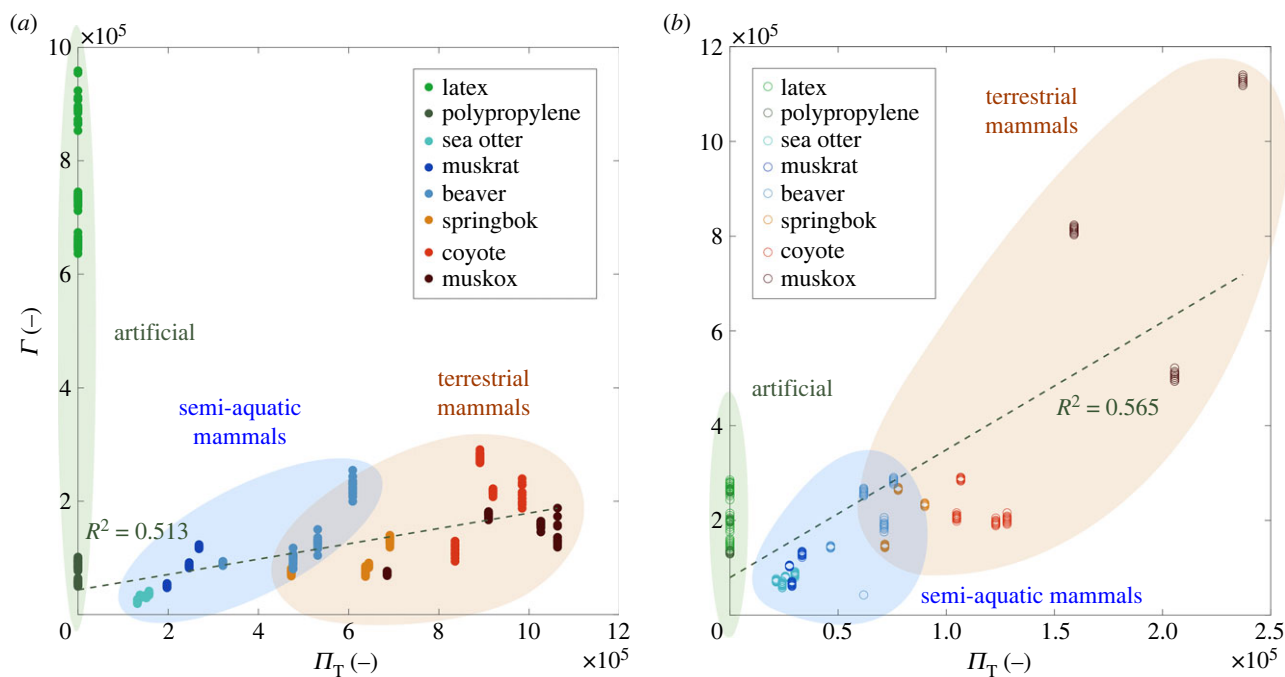


Figure 2. Non-dimensional fouling intensity Γ plotted against a group incorporating fibre characteristics, Π_T , in (a) flowing and (b) near-quiescent fowler streams. Data taken from Krsmanovic *et al.* [25].

different anti-fouling performances, as measured by N_p^* and revealed by a one-way analysis of variance on ranks, the Kruskal–Wallis statistical test [25]. The uniqueness guides the selection of a representative member from each of the three principal groups and reduces the number of required experiments. Polypropylene monofilaments (Textile Development Associates, Inc.) are used as a control and have a comparably smoother surface to our chosen hairs.

The fouling suspension is prepared by introducing TiO_2 powder (Pantai USA) into distilled water to achieve a TiO_2 mass concentration of 0.4 mg l^{-1} . Concentrations of TiO_2 of up to 0.2 mg l^{-1} cause visually observable deposition in less than an hour, and the concentration selected in these experiments produced satisfactory results in our previous work [25]. The suspension is Newtonian, $\mu = 0.94 \pm 0.02 \text{ cP}$, with majority of particles in sub- $5 \mu\text{m}$ range. The number of TiO_2 particles per millilitre of suspension N is measured with an optical density (OD) spectrophotometer (Digital Lab, model LDC 721), using a previously established polynomial fit [25],

$$N = -0.0186 \cdot \text{OD}_{600}^2 + 0.1169 \cdot \text{OD}_{600} + 0.0009. \quad (2.1)$$

Our preliminary tests show that 600 nm wavelength provides the most accurate spectrophotometer results over the whole range of measurements, compared with other wavelengths [25]. Therefore, our measurements are repeated here for optical density OD_{600} .

The dry TiO_2 powder has 0.05% residues on a $45 \mu\text{m}$ sieve, measured as per ISO 787-18 standard, according to the manufacturer (Pantai USA) [26]. Conventional TiO_2 nanoparticle diameter is approximately $O(2)$ smaller than the specified sieved material size [27–30]. Particulate aggregation size distribution in suspension is determined by sampling liquid from the experimental flow system—described below—running for 12 h. Three 0.2 ml samples are observed under a digital microscope (Keyence, model VHX-900) and images are processed using FIJI imaging software to identify the agglomerated TiO_2 particles. Approximately 74% of clumps have a projected area of less than or equal to $5 \mu\text{m}^2$. Clump sizing methodology and distribution images are provided in our previous work, Krsmanovic *et al.* [25].

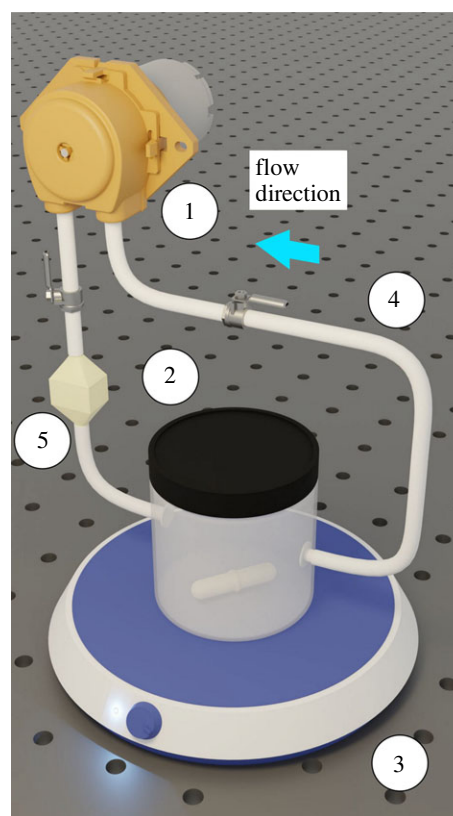


Figure 3. Schematic of the experimental system. A peristaltic pump (1) moves the fouling liquid from a reservoir (2) agitated by a magnetic stirrer (3) through tubing (4) in a closed loop. The sample mount (5) is oriented vertically in the closed system.

The experimental flow system circulates the TiO_2 suspension over fibre samples and is shown in figure 3. Peristaltic pump (1) (GOSO) draws the suspension from a 175 ml stock plastic reservoir (2) resting on a magnetic stirrer (3) (Chemglass Life Sciences, model OptiCHEM), which prevents settling and stratification of the suspension during the experiment. Three millimetre silicone tubing (4) delivers the suspension to a

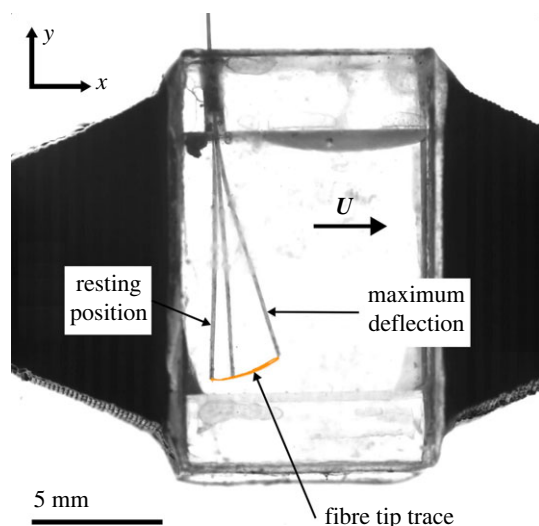


Figure 4. Shadowgraph of a transparent sample holder to show fibre deflection. Frames are superimposed to illustrate fibre flutter induced by a fouling liquid moving with velocity U .

custom three-dimensional-printed polylactide (PLA) fur sample mount (5). The TiO_2 suspension is circulated at a constant volumetric flow rate $Q = 40 \text{ ml min}^{-1}$. The mounts serve the dual purpose of sample holders and conduit connectors and are manufactured with equally spaced indentations at the parting line for sample placement. Fibres are affixed at one end and free at the other, thus forming cantilever beams, as shown in figure 4.

Two different lengths of the fibres are tested: 'long' cantilevers of approximately 9 mm, 'short' cantilevers of approximately 5 mm. Tabulated diameters and lengths for test fibres are provided in table 1. Cantilevered fibres stand in contrast to our previous work where the fibres were fixed at both ends, thus forming taut specimens [25]. The current sample mount (5) is modified from the previous study to create additional volume downstream of the mounting point to accommodate for fibre motion. The sample mount (5) is rigidly mounted to a wall physically separated from the pump using an inert base. The tubing is affixed upstream of the mount without affecting the net cross-sectional area, such that only vibrations administered by the liquid are received by the fibres.

Another version of the new mount, with the mounting chamber made from transparent acrylic, is manufactured to allow for high-speed imaging of fibre flutter, figure 4. We observe the fluttering motion of three fibre types by tracking the planar displacement of fibre tips, and log the tip coordinates 250 times per second to produce the temporal position of the fibre. A representative tip deflection time series and a frequency spectrum analysis are presented in figure 5.

For each experimental fouling trial, four fibres of one fibre type are selected from each of the three principal groups—polypropylene from artificial fibres, American beaver from semi-aquatic furs, and coyote from terrestrial furs—such that four like fibres are exposed to the fouling suspension simultaneously. Mammalian fibres are sampled from tanned pelts having no structural degradation observable under the scanning electron microscope (SEM) [25]. Hair samples are carefully affixed to sample mounts using ultraviolet (UV) curable adhesive so that the submerged portion of each fibre is not contaminated by glue. The UV-activated adhesive is then used to seal the sample mount seam. In each experiment, we circulate the fouling suspension in a closed loop over the fibres for 24 h, in the direction shown in figure 3. Upon the completion of one test, the mounts are separated at their seam, and the fibres are carefully trimmed from their glued base using curved, stainless steel scissors. The fibre samples are placed in a semi-micro 3 ml cuvette

(BrandTech), full of 1 ml of distilled water using an adjustable volume pipette dispenser (Four E's Scientific). The cuvette is placed in an ultrasonic cleaner (Isonic), and the bath water level and cleaning programme are selected as per manufacturer recommendations for samples in a dedicated container. The procedure ensures complete removal of attached TiO_2 particles as demonstrated in Krsmanovic *et al.* [25]. After removal from the ultrasonic bath, the cuvette is dried with Kimwipes to ensure exterior walls are kept free of contaminants that could disrupt OD measurement. The spectrophotometer is calibrated by measuring the OD of a cuvette filled with 1 ml of distilled water. Three OD measurements are taken for each sample.

3. Experimental results and discussion

We expose triplets of mammalian and synthetic fibres to a pulsatile colloid flow carrying TiO_2 particles for 24 h. In our previous work [25], we carried out a one-way statistical analysis of variance on ranks to identify statistically dissimilar anti-fouling behaviour between different fibre types. While certain fibre pairs exhibited similar receptiveness to fouling, the majority of pairs demonstrated individual affinities to the accumulation of foreign matter. Based on the pairwise results, we identify three fibres as representative for each principal group: polypropylene for artificial fibres, beaver for semi-aquatic mammal fur and coyote for terrestrial mammal fur. The differences in anti-fouling performance between the different pairs, measured by the normalized number of attached particles [25] N^*_p , are determined with the significance of $p = 0.019$ for polypropylene–beaver pair, and $p = 0.000$ polypropylene–coyote and for beaver–coyote pairs.

The flow rate Q generated by our pump creates an average velocity $U \approx 10 \text{ cm s}^{-1}$ and Reynolds number $\text{Re}_D = \rho U D / \mu \approx 10$ over a $D = 80 \mu\text{m}$ circular cylinder, corresponding to laminar flow with two attached vortices. This estimate of Reynolds number does not account for fibre deflection by hydrodynamic drag and deviation from circularity in the fibre cross-section, as noted previously [25]. Deflection both changes the angle of incidence and true Re_D value along the fibre length. The inherent unsteadiness in the peristaltic pump and vortex shedding in the fibre wake causes the fibres to oscillate in the flow field. To characterize this oscillation, the temporal position of the fibre tip is tracked optically for a brief trial in the transparent flow cell pictured in figure 4. A representative 4 s waveform diagram of fibre tip displacement in x is plotted in figure 5a, and shows no discernible periodicity unless smoothed aggressively by a second-order Savitsky–Golay filter. The smoothed, red track in figure 5a shows a higher frequency wave superimposed on an approximately 2 Hz wave for the sample beaver fibre. Power-spectral analysis and a fast Fourier transform on the raw signal indicate an 18.6–18.7 Hz dominant frequency, as shown on figure 5b. We posit the dominant frequency is a result of fluid–structure interactions, while the 2 Hz vibration is a result of the peristaltic pulsing in the bulk flow. Neither of the detected dominant frequencies matches the expected Strouhal (St) frequency of vortex shedding from a rigid cylinder located in a fully developed, uniform, laminar flow, $f = \text{St}U/D \approx 160 \text{ Hz}$, where $\text{St}(\text{Re} = 10) \approx 0.16$. Such a mismatch is no surprise since cantilevered fibre motion is driven by the fluid–structure coupled dynamics, whereas the diffusion of flow from a circular tube to the rectangular sample holder may have a significant effect on shedding frequency

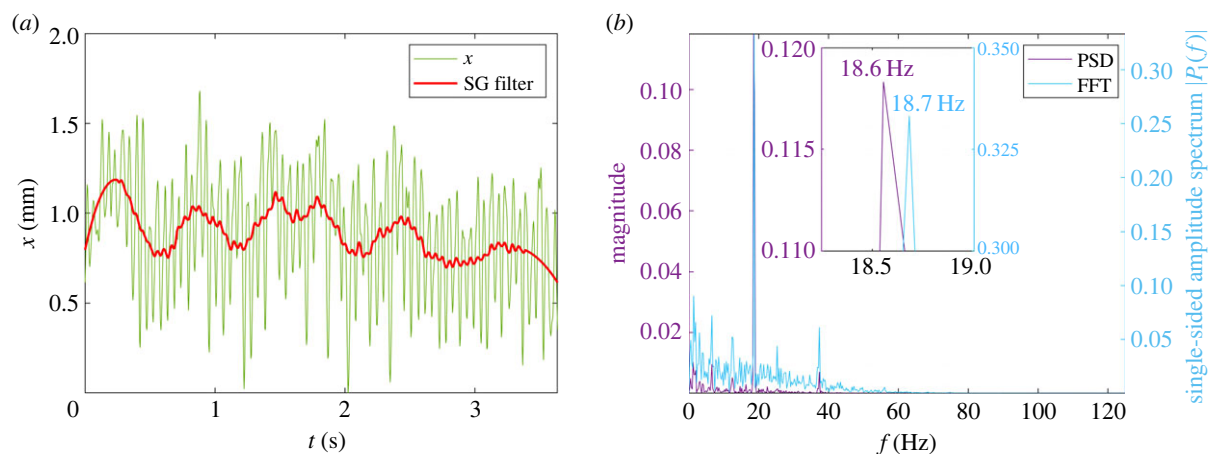


Figure 5. Cantilevered American beaver fibre oscillations in flow. (a) Raw lateral deflection (green) is filtered (red) for a 4 s duration experiment. (b) A power-spectral analysis (PSD, purple) and a fast Fourier transform (FFT, blue) agree on the dominant frequency of the filtered signal.

Table 1. Experimental fibre types, dimensions and averaged fouling measurements.

material	cantilever	hydraulic diameter (μm)	average length (mm)	OD_{600}	$\bar{N}_p, 10^8$ (—)	$\bar{N}_p^*, 10^7$ (mm^{-2})
polypropylene	long	69.5	8.863	0.027 ($n = 40$)	0.802	1.054
	short	70.1	5.125	0.053 ($n = 40$)	1.410	3.128
beaver	long	80.0	8.965	0.049 ($n = 40$)	1.103	1.220
	short	78.2	4.939	0.061 ($n = 40$)	1.606	3.577
coyote	long	60.8	9.128	0.065 ($n = 40$)	1.677	2.464
	short	71.4	4.514	0.065 ($n = 40$)	1.696	4.286

[31]. The remaining two types of fibres tested in the see-through flow cell exhibit similar quasi-repetitive type of motion. The relation between flexible fibre dynamics and Reynolds number across various scales is a fruitful area for future work and a complete description is beyond the scope of this study.

The spanwise variation in the angle of incidence and wake structure of long, short and fibres fixed at both ends are likely to influence local fouler attachment. Such rates of attachment are further impacted by the build-up, and sloughing, of fouler aggregates [23]. Thus, a temporal characterization of fouling down the fibre length is difficult to attain. Instead, we measure fouling intensity by removing all TiO_2 from a fibre and counting the resultant particles. A tabulated summary of the average number of particles \bar{N}_p collected by the various fibre types is presented in table 1. Coyote fur fibres collected the greatest number of particles for both long and short cantilever categories, while polypropylene collected the least. The number of particles collected per unit surface area N_p^* allows us to compare fibres of different diameters and lengths, a term we dub fouling intensity. We present values of N_p^* graphically for fibres fixed at both ends (previous work) in figure 6a, and results from the present cantilevers in figure 6b,c. Averaged values of fouling intensity for all trials \bar{N}_p^* are given in table 1.

Fibres fixed at both ends collect more particles per unit area in a 24 h period than those cantilevered, as shown by comparing figure 6a with figure 6b,c. The decrease in \bar{N}_p^* between fibres fixed at both ends and the long cantilevers is solely the result of releasing one of the fibre ends. The fouling intensity N_p^* recovers as the fibre is made shorter and,

thus, stiffer (figure 6c). In all cases, fixed, long and short, the fouling intensities of fibres relative to each other remain fairly consistent, with the beaver and the polypropylene fibres fouling notably less than coyote. Coyote fur propensity for fouling, in relation to the other two, is perhaps unsurprising in light of its land-dwelling nature. We posit the lesser degree of fouling experienced by cantilevered fibres is due to two physical reasons: (i) bent fibres greatly reduce flow stagnation from a stagnation line in rigid fibres to a point, and (ii) fibre deformation strains the solid surface, thereby defeating particulate adhesion. Adhesion to a surface is the net result of surface attractive (e.g. van der Waals, electrostatic) and repulsive (elastic) forces [32]. Additional repulsive forces can arise from inertial body forces of vibration. In the present case, the straining of fibres creates additional elastic forces from both bending and potentially increased tension in the fibres from extension. This latter extensional effect is a well-known membrane stiffening effect (Foppl-von Karman strains) and tends to become significant at 10 – 15° of beam rotation [33]. In our current problem, assuming a uniformly loaded cantilever and Euler–Bernoulli bending as a first-order estimate, we calculate beam rotation $\theta = 4x/3L \approx 1/6$ rad or approximately 10° , where L is fibre length. This beam rotation can lead to appreciable membrane stiffening to develop, and on thin and ultra-thin beams, it leads to both an increase in stiffness and natural frequency during forced vibrations [34,35]. Evidence of these two mechanisms (i, ii) lies in the observation that longer cantilevers, undergoing the most deformation, have lower values of \bar{N}_p^* , as shown by figure 6b,c. The shorter cantilevers behave more like those fixed at both ends.

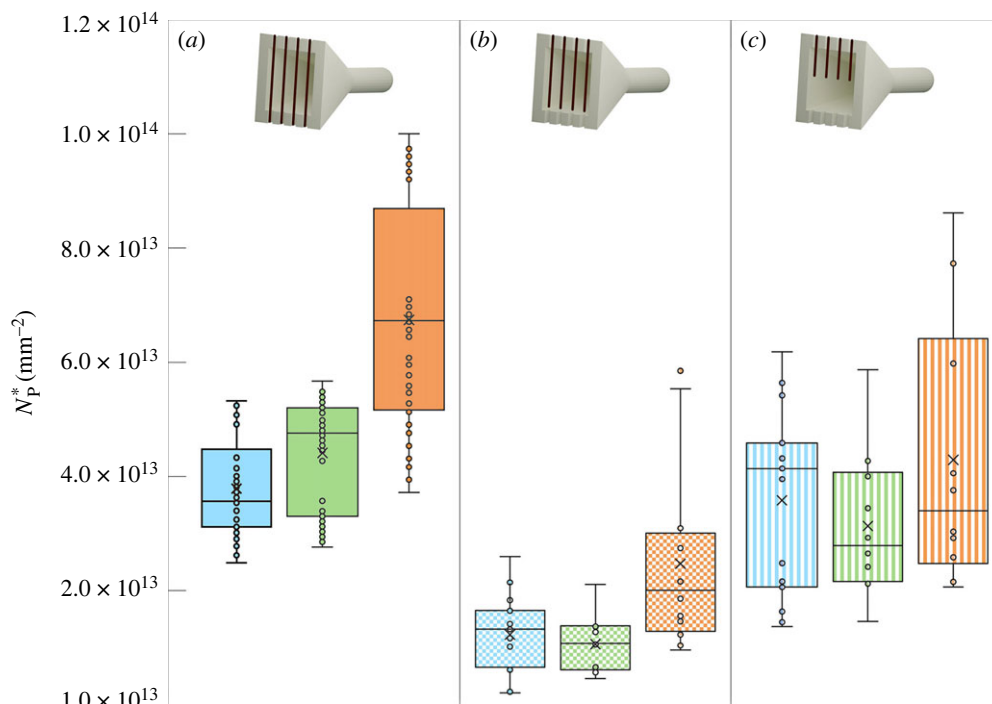


Figure 6. Fouling intensity N_p^* values for (a) fibres taut at both ends (previous work), (b) long cantilever and (c) short cantilever. Blue: American beaver; green: polypropylene, orange: coyote.

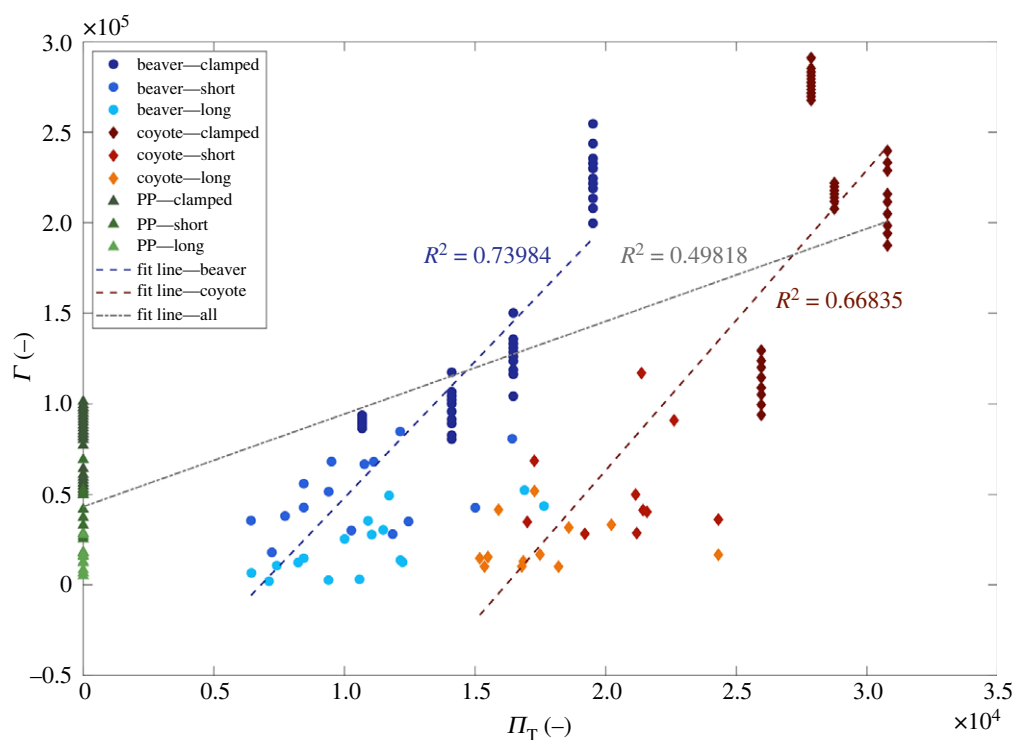
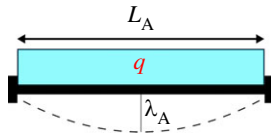
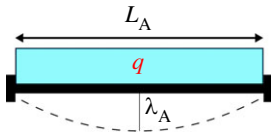
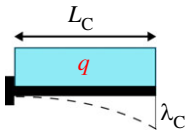


Figure 7. Non-dimensional Π -term correlations for the three fibre groups, excluding the deflection ratio term λ^* . Dashed lines designate the correlation trend lines for individual animal fur groups, and dash-dot for all tested fibres.

We repeat the non-parametric test on ranks, and make a similar discovery as in our previous work: the groups differ in their anti-fouling performance, both when observing the two cantilevered configurations alone, $\chi^2 = 12.680$, $p = 0.027$, and when the two configurations are compared with the fibres fixed at both ends we previously tested, $\chi^2 = 129.136$, $p = 0.000$. We determine the critical value of χ^2 for the given degrees of freedom [36], d.f. = $3 - 1 = 2$, and significance

level, $p = 0.050$, to be $\chi_{cr}^2 = 5.5991$, and note that χ^2 value for cantilevered fibres is an order of magnitude lower than the χ^2 value for fibres fixed at both ends, and as such approaches the critical value. The level of significance calculated for the cantilevered configurations alone indicates that similarity in anti-fouling behaviour increases as fibres become free to flutter in flow, emphasizing the importance of flexing motion compared with the other morphological factors.

Table 2. Comparison of beam configurations and deflection ratio λ^* .

beam configuration	fixed	long cantilever	short cantilever
			
beam length	$L_A = L$	$L_B = L$	$L_C = 0.5L$
maximum theoretical deflection	$\lambda_A = qL^4/384EI$	$\lambda_B = qL^4/8EI$	$\lambda_C = qL^4/128EI$
deflection ratio	$\lambda_A^* = \lambda_A/\lambda_A = 1$	$\lambda_B^* = \lambda_B/\lambda_A = 48$	$\lambda_C^* = \lambda_C/\lambda_A = 3$

The ability of our previously derived scaling relation given by equations (1.2) and (1.3) is shown in figure 7. For cantilevered fibres (1.3) performs well for isolated fibre types, semi-aquatic and terrestrial, but poor globally, with $R^2 = 0.498$. Such a result suggests that flow-induced deformation is significant and should be represented in our non-dimensional parameter analysis. The inclusion of flow-induced deformation requires that we first non-dimensionalize the deflection enabled by a free fibre end. We compare the flexing behaviour of cantilevered fibres in a uniform flow with the previous study case, fibres fixed at both ends [25]. We assume that the drag-induced pressure q , an analogue to a static uniform distributed load on an ideal beam, is identical for all tested filaments laying at the neutral plane. Long cantilevers have the same length as fibres fixed at both ends, $L_A = L_B = L$. The short cantilevers have length $L_C = 0.5L$. Our comparative analysis does not require we define the fibre stiffness EI . We observe the maximum theoretical deflection [37], λ , that can be realized by applying q , as shown for each fibre in table 2, and normalize it against the base case of a fixed beam. By doing so, we establish a non-dimensional parameter, in a manner similar to how we established others [25] in (1.1), and obtain a comparative measure of additional freedom of movement a fibre gains with a free end and varying length. We label this parameter the deflection ratio λ^* and calculate its values as shown in table 2. The values of λ^* indicate that long cantilevers experience deflection 16 \times greater than a short cantilever and 48 \times more than a fixed fibre.

Deflection ratio λ^* can be incorporated into our $\Gamma \sim \Pi_T$ relation (1.3) to account for fibre rigidity. Since we observe a reduction in fouling intensity, N_P^* , for an increase in fibre mobility, we choose to include λ^* in the denominator of Π_T , resulting in the updated expression,

$$\underbrace{N_P^* \cdot \left(\frac{1}{R}\right)^{-2}}_{\Gamma} \sim \underbrace{\text{Re}_R \left(\frac{1}{R}\right)^{-2} \text{Oe} \left(\frac{\tau_w}{\rho U}\right)}_{\Pi_\lambda} t_c (\lambda^*)^{-1}. \quad (3.1)$$

Non-dimensional $\Pi_T = \Pi_\lambda$ for fibres fixed at both ends. The renewed correlation given by (3.1) is fit to experimental data in figure 8. We observe trend-line agreement for our two individual fur groups, and a coefficient of determination $R^2 = 0.71$ when polypropylene fibres are included, indicating that fibre motion is indeed a significant factor. The correlation coefficient R^2 is increased by approximately 40% compared with the original work (figure 7) when fibres are free to move in flow. The difference in the coefficient of

determination R^2 between the dash-dot trend lines on figures 7 and 8 describes how strongly λ^* influences the filament anti-fouling performance. Fibre movement more significantly affects resistance to fouling than other passive characteristics, such as surface feature size ϵ or circularity \emptyset . The demarcation between the different fibre groups, imposed by morphology, as seen in figure 2 is now lost in figure 8. The trends shown in figure 8 are statistically supported by the results of bivariate correlation analysis which confirms a high level of interdependence between Γ and Π_λ , $r(293) = 0.844$, $p = 0.000$. The value of $r = 0.844$ is higher compared with any of those we discovered in the preceding investigation of rigid samples between the values of Γ and Π_T , (1.3). As fibres become free to move, morphological differences between furs become less significant. Freedom of movement is, therefore, a unifying characteristic across classes. Fur arranged in pelts may be more restricted to flutter than the fibres tested here, but we posit that mechanical contact with neighbouring fibres is an effective means for removing deposition. For singular fibres, segregation in performance is driven by fibre length, that is—rigidity. We can imagine that factors from other groups [8] such as genotypic, temporal or factors of random attachment and detachment may further improve the correlations described here; however, we are currently unable to anticipate which non-physico-mechanical factors will be significant for such grouping. The inclusion of elements pertaining to other disciplines—biological, genetic, chemical and so on—into a unifying analysis, will further improve our understanding of the synergistic effects of fur anti-fouling performance. For example, it is unknown if the secretion of sebum oils contributes to the absence of foulers, or if the keratinous structure of hair inhibits chemical or other reactions required for foulers to successfully attach and proliferate. Gaining insight into the combined effects of such diverse factors could establish a ‘grand unified theory’ of fur anti-fouling behaviour.

In our previous work [25], we contemplate that anti-fouling characteristics of fur are perhaps just a serendipitous evolutionary by-product, given that the primary functions of fur include thermal insulation via air-entrapment, camouflage and protection [38]. While the shorter, dense underfur maintains an insulating layer of air, sparse guard hair arrests incident heat flux and deflects precipitation [39,40]. Guard hair is water repellent [41,42], provides protection from felting for the underfur [43], and has the capability to transmit sensory feedback [44,45] due to enhanced freedom of movement compared with the tight undercoat [46]. If the function of the fur patch closest to the body is to trap the

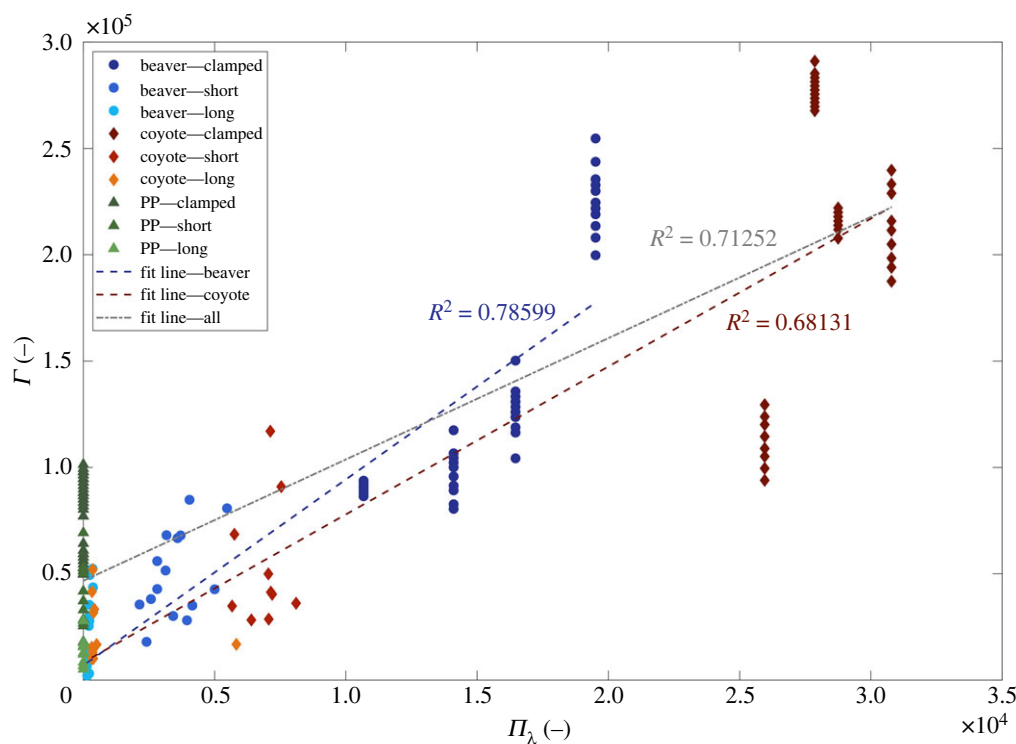


Figure 8. Non-dimensional II -term correlations for the three fibre groups, including the deflection ratio term λ^* . The lines designate correlation trend lines.

air, and thus the heat, flexing guard fur strands protruding above the underfur not only facilitates physical protection of the underfur, heat retention and water repellence, but also enables continuous active shedding of foulers, without disruption of the insulating layer. If guard hair, or underfur for mammals that possess it, were to foul, the arrangement of a pelt would be locally disrupted. The inclusion of foreign matter would probably increase pelt thermal conductivity, increase drag coefficients in swimming semi-aquatic mammals, retain additional water as mammals emerge from a bath, and decrease the effectiveness of shaking to dry [42]. Water retention increases both the energetic cost of locomotion and heat loss. Therefore, the fouling of fur may be detrimental across multiple functional domains.

Our work investigates the previously unknown physico-mechanical factors enabling passive fur anti-fouling. By focusing on the particular physical parameters we aim to not only reveal the obscured physics, but also to describe parameters of greatest importance that would enable replication, and ultimately manufacturing, of filamentous, anti-fouling structures. The significant improvement of our initial findings may serve as an invitation to other researchers outside of our domain of expertise to expand the research to other factors contributing to such a complex process. Understanding the synergistic influence of genotypic, deterministic or import-export factors [23] may further improve our knowledge of a manifestly fouling-resistant system, and enable a more feasible manufacturing of passive anti-fouling surfaces robust to a range of applications.

4. Conclusion

In this study, we expose cantilevered fibres of beaver and coyote fur, and polypropylene to TiO_2 -rich stream. The TiO_2 particles are collected by the fibres over a 24 h period. Cantilevered fibres collect fewer particles per unit area than

fibres fixed at both ends. Longer fibres, which can deflect or flutter in flow to a greater extent, collect fewer particles per unit area. Thus, at the scale of these slender fibres, static substrates are more susceptible to fouling by titanium oxide, an observation that is probably extendable to other foulers. The fluid-structure interactions in our system are coupled and largely uncharacterized, but we infer that fibre flexibility reduces stagnation and increases surface strain, thereby resisting foulers. The anti-fouling behaviour of fur is complex and cannot be predicted by a single system parameter. Instead, we find a dimensionless group that incorporates the ability of the fibre to deflect, flow characteristics of the surrounding fluid, and surface features that enable us to predict fouling intensity.

Ethics. This work did not require ethical approval from a human subject or animal welfare committee.

Data accessibility. Raw Experimental data are available from Open Science Framework repository: <https://osf.io/5bp2v/?> [47].

Declaration of AI use. We have not used AI-assisted technologies in creating this article.

Authors' contributions. M.K.: conceptualization, data curation, formal analysis, investigation, methodology, validation, visualization, writing—original draft, writing—review and editing; R.G.: conceptualization, funding acquisition, project administration, resources, supervision, writing—review and editing; A.K.D.: conceptualization, funding acquisition, investigation, project administration, resources, supervision, writing—original draft, writing—review and editing.

All authors gave final approval for publication and agreed to be held accountable for the work performed therein.

Conflict of interest declaration. We declare we have no competing interests.

Funding. The authors acknowledge the National Science Foundation (grant no. CMMI-1825801) for funding this work.

Acknowledgements. The authors would like to thank Peter Schmitt of Textile Development Associates, Inc. for supplying polypropylene monofilaments. M.K. would like to thank Dr Hessein Ali for valuable discussions related to filament particles deposition.

References

- Lappin-Scott HM, Costerton JW. 1989 Bacterial biofilms and surface fouling. *Biofouling* **1**, 323–342. (doi:10.1080/08927018909378120)
- Watkinson AP, Panchal CB. 1990 A critical review of organic fluid fouling. *AIChE summer meeting, San Diego, CA*.
- Bott TR. 1995 *Fouling of heat exchangers*. Amsterdam, The Netherlands: Elsevier. (doi:10.1016/B978-0-444-82186-7.X5000-3)
- Goode KR, Asteriadou K, Robbins PT, Fryer PJ. 2013 Fouling and cleaning studies in the food and beverage industry classified by cleaning type. *Compr. Rev. Food Sci. Food Saf.* **12**, 121–143. (doi:10.1111/1541-4337.12000)
- Park J, Yamashita N, Tanaka H. 2018 Membrane fouling control and enhanced removal of pharmaceuticals and personal care products by coagulation-MBR. *Chemosphere* **197**, 467–476. (doi:10.1016/j.chemosphere.2018.01.063)
- Yu W-z, Qu J-h, Gregory J. 2015 Pre-coagulation on the submerged membrane fouling in nano-scale: effect of sedimentation process. *Chem. Eng. J.* **262**, 676–682. (doi:10.1016/j.cej.2014.09.102)
- Wingender J, Neu TR, Flemming H-C. 1999 *What are bacterial extracellular polymeric substances?* Berlin, Germany: Springer.
- Wimpenny J, Manz W, Szewzyk U. 2000 Heterogeneity in biofilms. *FEMS Microbiol. Rev.* **24**, 661–671. (doi:10.1111/j.1574-6976.2000.tb00565.x)
- Rho H, Kim S, Shin J, Cho J, Lee Y-G, Chon K. 2022 Effects of two-step cleaning sequences on foulant extraction from multibore ultrafiltration membranes in a pilot-scale membrane filtration system for surface water treatment. *Chemosphere* **297**, 134164. (doi:10.1016/j.chemosphere.2022.134164)
- Gul A, Hruza J, Yalçinkaya F. 2021 Fouling and chemical cleaning of microfiltration membranes: a mini-review. *Polymers* **13**, 846. (doi:10.3390/polym13060846)
- Arefi-Oskoui S, Khataee A, Safarpour M, Orooji Y, Vatanpour V. 2019 A review on the applications of ultrasonic technology in membrane bioreactors. *Ultrason. Sonochem.* **58**, 104633. (doi:10.1016/j.ultsonch.2019.104633)
- Terán Hilarés R, Singh I, Tejada Meza K, Colina Andrade GJ, Pacheco Tanaka DA. 2022 Alternative methods for cleaning membranes in water and wastewater treatment. *Water Environ. Res.* **94**, e10708. (doi:10.1002/wer.10708)
- Kalumuck KM, Chahine GL, Frederick GS, Aley PD. 1997 Development of a dynajet cavitating water jet cleaning tool for underwater marine fouling removal. In *9th American Waterjet Conf., Dearborn, Michigan*.
- Karlsson J, Eklund B. 2004 New biocide-free antifouling paints are toxic. *Mar. Pollut. Bull.* **49**, 456–464. (doi:10.1016/j.marpolbul.2004.02.034)
- Lejars M, Margailan A, Bressy C. 2012 Fouling release coatings: a nontoxic alternative to biocidal antifouling coatings. *Chem. Rev.* **112**, 4347–4390. (doi:10.1021/cr200350v)
- Bixler GD, Theiss A, Bhushan B, Lee SC. 2014 Anti-fouling properties of microstructured surfaces bio-inspired by rice leaves and butterfly wings. *J. Colloid Interface Sci.* **419**, 114–133. (doi:10.1016/j.jcis.2013.12.019)
- Liang Y, Yang E, Kim M, Kim S, Kim H, Byun J, Yanar N, Choi H. 2023 Lotus leaf-like SiO₂ nanofiber coating on polyvinylidene fluoride nanofiber membrane for water-in-oil emulsion separation and antifouling enhancement. *Chem. Eng. J.* **452**, 139710. (doi:10.1016/j.cej.2022.139710)
- de Beer D, Stoodley P. 1995 Relation between the structure of an aerobic biofilm and transport phenomena. *Water Sci. Technol.* **32**, 11–18. (doi:10.2166/wst.1995.0252)
- Stewart PS. 2012 Mini-review: convection around biofilms. *Biofouling* **28**, 187–198. (doi:10.1080/08927014.2012.662641)
- Damodaran VB, Murthy NS. 2016 Bio-inspired strategies for designing antifouling biomaterials. *Biomater. Res.* **20**, 1–11. (doi:10.1186/s40824-016-0064-4)
- Li Z, Guo Z. 2019 Bioinspired surfaces with wettability for antifouling application. *Nanoscale* **11**, 22 636–22 663. (doi:10.1039/C9NR05870B)
- Lewin RA, Farnsworth PA, Yamanaka G. 1981 The algae of green polar bears. *Phycologia* **20**, 303–314. (doi:10.2216/i0031-8884-20-3-303.1)
- Krsmanovic M, Biswas D, Ali H, Kumar A, Ghosh R, Dickerson AK. 2021 Hydrodynamics and surface properties influence biofilm proliferation. *Adv. Colloid Interface Sci.* **288**, 102336. (doi:10.1016/j.cis.2020.102336)
- Umphreys T. *American beaver*. See <https://unsplash.com/photos/s7ZABNRG2bw>.
- Krsmanovic M, Ali H, Biswas D, Ghosh R, Dickerson AK. 2022 Fouling of mammalian hair fibres exposed to a titanium dioxide colloidal suspension. *J. R. Soc. Interface* **19**, 20210904. (doi:10.1098/rsif.2021.0904)
- Pantai ptr-620 titanium dioxide product information*. See <https://web.archive.org/web/20210514095831/>. <https://www.pantaiusa.com/product-page/pantai-ptr-620-titanium-dioxide-tio2-1-lb> (accessed 29 January 2022).
- Winkler J. 2014 *Titanium dioxide: production, properties and effective usage*, 2nd revised edn. Hannover, Germany: Vincentz Network.
- Shi H, Magaye R, Castranova V, Zhao J. 2013 Titanium dioxide nanoparticles: a review of current toxicological data. *Part. Fibre Toxicol.* **10**, 1–33. (doi:10.1186/1743-8977-10-15)
- Xu G, Zhang J, Song G. 2003 Effect of complexation on the zeta potential of titanium dioxide dispersions. *J. Dispers. Sci. Technol.* **24**, 527–535. (doi:10.1081/DIS-120021807)
- Geiss O *et al.* 2021 Particle size analysis of pristine food-grade titanium dioxide and E 171 in confectionery products: interlaboratory testing of a single-particle inductively coupled plasma mass spectrometry screening method and confirmation with transmission electron microscopy. *Food Control* **120**, 107550. (doi:10.1016/j.foodcont.2020.107550)
- Schwinge J, Wiley DE, Fletcher DF. 2003 Simulation of unsteady flow and vortex shedding for narrow spacer-filled channels. *Ind. Eng. Chem. Res.* **42**, 4962–4977. (doi:10.1021/ie030211n)
- Johnson KL, Johnson KL. 1987 *Contact mechanics*. Cambridge, UK: Cambridge University Press.
- Reddy JN. 2007 Nonlocal theories for bending, buckling and vibration of beams. *Int. J. Eng. Sci.* **45**, 288–307. (doi:10.1016/j.iijengsci.2007.04.004)
- Ghosh R, Mukherjee S. 2009 Fully Lagrangian modeling of dynamics of MEMS with thin beams—part I: undamped vibrations. *J. Appl. Mech.* **76**, 051007. (doi:10.1115/1.3086785)
- Ghosh R, Mukherjee S. 2009 Fully Lagrangian modeling of dynamics of MEMS with thin beams—part II: damped vibrations. *J. Appl. Mech.* **76**, 051008. (doi:10.1115/1.3086786)
- Wilson EB, Hilferty MM. 1931 The distribution of chi-square. *Proc. Natl Acad. Sci. USA* **17**, 684–688. (doi:10.1073/pnas.17.12.684)
- Budynas RG, Nisbett JK. 2011 *Shigley's mechanical engineering design*, vol. 9. New York, NY: McGraw-Hill.
- Sokolov VE 1982 *Mammal skin*. Berkeley, CA: University of California Press.
- Kelt DA, Patton JL. 2020 *A manual of the mammalia: an homage to Lawlor's 'handbook to the orders and families of living mammals'*. Chicago, IL: University of Chicago Press. **103**, 222–224. (doi:10.1093/jmammal/gyab136)
- Fish FE, Smelstoy J, Baudinette RV, Reynolds PS. 2002 Fur doesn't fly, it floats: buoyancy of pelage in semi-aquatic mammals. *Aquat. Mamm.* **28**, 103–112.
- Akademia Nauk SSSR, Consultants Bureau Enterprises and Consultants Bureau. 1987 *Doklady: Biophysics nos. 292–297; v. 292*. See <https://books.google.com/books?id=OpUhaQAAMAAJ>.
- Dickerson AK, Mills ZG, Hu DL. 2012 Wet mammals shake at tuned frequencies to dry. *J. R. Soc. Interface* **9**, 3208–3218. (doi:10.1098/rsif.2012.0429)
- Guzman-Solis A, Elorriaga-Verplancken F, Acevedo-Whitehouse K. 2023 Guadalupe fur seal alopecia: a metabolic syndrome associated to climatic anomalies? *bioRxiv*. (doi:10.1101/2023.04.02.535308)
- Baker IM. 2021 Infrared antenna-like structures in mammalian fur. *R. Soc. Open Sci.* **8**, 210740. (doi:10.1098/rsos.210740)
- Masterton R. 2013 *Sensory integration*, vol. 1. New York, NY: Springer Science & Business Media. (doi:10.1007/978-1-4684-2730-1)
- Kaplan H. 2013 *Furskin processing: the Commonwealth and International Library: leather technology*. Amsterdam, The Netherlands: Pergamon.
- Krsmanovic M, Ghosh R, Dickerson AK. 2023 Data from: Fur flutter in fluid flow feeds off foulers. OSF repository. (<https://osf.io/5bp2v/>)